



HAL
open science

Oxygen non-stoichiometry phenomena in $\text{Pr}_{1-x}\text{Zr}_x\text{O}_{2-y}$ compounds ($0.02 < x < 0.5$).

Jonathan Abel, Mélanie Majimel, Jérôme Majimel, V. Bellière-Baca, V. Harlé, Gilles André, Carmelo Prestipino, Santiago Figueroa, Etienne Durand, Alain Demourgues

► **To cite this version:**

Jonathan Abel, Mélanie Majimel, Jérôme Majimel, V. Bellière-Baca, V. Harlé, et al.. Oxygen non-stoichiometry phenomena in $\text{Pr}_{1-x}\text{Zr}_x\text{O}_{2-y}$ compounds ($0.02 < x < 0.5$).. Dalton Transactions, 2014, 43 (40), pp.15183-15191. 10.1039/c4dt01545b . hal-01072100

HAL Id: hal-01072100

<https://hal.science/hal-01072100>

Submitted on 22 Jun 2022

HAL is a multi-disciplinary open access archive for the deposit and dissemination of scientific research documents, whether they are published or not. The documents may come from teaching and research institutions in France or abroad, or from public or private research centers.

L'archive ouverte pluridisciplinaire **HAL**, est destinée au dépôt et à la diffusion de documents scientifiques de niveau recherche, publiés ou non, émanant des établissements d'enseignement et de recherche français ou étrangers, des laboratoires publics ou privés.

Oxygen non-stoichiometry phenomena in $\text{Pr}_{1-x}\text{Zr}_x\text{O}_{2-y}$ compounds ($0.02 < x < 0.5$)

J. Abel,^a M. Lamirand-Majimel,^a J. Majimel,^a V. Bellière-Baca,^b V. Harlé,^b G. André,^c C. Prestipino,^d S. Figueroa,^e E. Durand^a and A. Demourgues^{*a}

New $\text{Pr}_{1-x}\text{Zr}_x\text{O}_{2-y}$ oxides with $x < 0.5$ have been prepared by co-precipitation in basic medium and annealed under air at high temperatures ($T \leq 1200$ °C). Defined compositions with $x = 0.02, 0.1, 0.2, 0.35, 0.40$ and 0.5 have been characterized by XRD, Zr-K-edge EXAFS for the local structure, magnetic susceptibility measurements, and Pr L_{III}-edge XANES in order to identify the variation of the cell parameter and Zr local environment versus Zr content and Pr^{n+} ($4 < n < 3$) oxidation states. The higher the Zr content, the lower the Pr valence state. The Zr amount stabilized in the distorted octahedral site is at the origin of the formation of defined compositions as discovered by Leroy Eyring *et al.* in the $\text{Pr}_n\text{O}_{2n-2m}$ series and the generation of oxygen vacancies stabilized in the fluorite-type network. TGA and TPR analyses help to follow the reduction properties under Ar/5% H₂ and show high Pr reducible rates at low temperatures ($T < 250$ °C). The identification of the fluorite-type superstructure (SG: $1a\bar{3}$) of reduced compositions annealed at $T = 900$ °C under Ar/5% H₂ shows the cationic and oxygen vacancy ordering. This feature plays a key role with Zr^{4+} cations stabilized in flattened octahedral sites for the generation of oxygen vacancies and the stabilization of Pr^{3+} in the reduced states.

DOI: 10.1039/XXXXXXXXXX

Introduction

Rare earth-based oxides have been widely investigated considering various compositions and structural features related to ionic and redox properties for numerous applications such as catalytic oxidation^{1,2} or fuel cells.³ Those applications require materials which exhibit high oxygen mobility and redox properties at low temperatures associated with oxygen non-stoichiometry or vacancies and mixed valence states. Ceria (CeO_2) being well established as an oxygen buffer is widely used in catalysis in which oxidation–reduction processes are involved.⁴

Ceria–zirconia mixed oxide materials have been developed as Three-Way-Catalysts (TWCs) and exhibit high oxygen storage capacity (OSC) with high oxygen release under reducing conditions and fast kinetics, high content of reducible Ce^{4+} at $T < 600$ °C, and high thermal stability with good surface areas between 20 and 40 m² g⁻¹ stabilized at $T > 1000$ °C. Various networks such as fluorite-type for high Ce rate, tetragonal dis-

tortion of the fluorite-type structure for high Zr content and the pyrochlore-type structure^{8–19} for equimolar compositions have been characterized in the last 20 years.^{5–10} The pyrochlore corresponding to a fluorite-type superstructure with $\text{Ce}^{4+}/\text{Ce}^{3+}$, eight-fold coordinated to oxygens and Zr^{4+} cations in a distorted octahedral site as well as oxygen vacancy ordering exhibit the best redox properties.¹⁸ Then the occurrence of cation site distortions as well as cationic ordering plays a key role for OSC, Ce reducibility and minimum temperature of reduction.¹⁸

However, Pr-based oxides should be able to compete with Ce-based oxides.¹¹ Pr $[\text{Xe}] 6s^2 4f^3 5d^0$ has got one electron more than Ce $[\text{Xe}] 6s^2 4f^2 5d^0$. Its most stable defined compounds are Pr_7O_{12} (ref. 12) and $\text{Pr}_{24}\text{O}_{44}$ (Pr_6O_{11})¹³ containing mixed $\text{Pr}^{4+}/\text{Pr}^{3+}$ valence states. The $\text{Pr}_n\text{O}_{2n-2m}$ defect structures were extensively studied by Eyring *et al.*¹⁴ Considering ionization energies of Pr and Ce, Pr^{4+} is less stable and more reducible than Ce^{4+} . Moreover, in solution, the redox potential $\text{Pr}^{4+}/\text{Pr}^{3+}$ is larger and equal to 2.7 V per ENH than that of $\text{Ce}^{4+}/\text{Ce}^{3+}$ equal to 1.7 V per ENH. Hence, $\text{Pr}_{1-x}\text{Zr}_x\text{O}_{2-y}$ solid solutions are expected to exhibit mixed valence states and oxygen vacancies associated with oxygen mobility and redox processes at low temperatures.

In previous studies,^{15,16} no information has been given on Pr valence states in the oxidized as well as reduced phases. Moreover, no structural features of reduced compounds have been investigated and finally no defined compound (thermo-

^aCNRS, Université de Bordeaux 1, ICMCB, 87 avenue du Dr. Albert Schweitzer, 33608 Pessac, France. E-mail: demourg@icmcb-bordeaux.cnrs.fr

^bSOLVAY, RIC, 52 rue de la Haie Coq, 93308 Aubervilliers Cedex, France

^cCEA, IRAMIS, LLB, 91191 Gif-sur-Yvette Cedex, France

^dCNRS, Université de Rennes 1, SCR, Campus de Beaulieu – Bâtiment 10B, 263 avenue du Général Leclerc, 35042 Rennes Cedex, France

^eESRF, 6, rue Jules Horowitz, 38000 Grenoble, France

dynamically stable) has been characterized or discussed in this series.

Narula *et al.*¹⁵ reported the synthesis, structure and redox properties of $\text{Pr}_{1-x}\text{Zr}_x\text{O}_{2-y}$ ($x = 0.25, 0.5$ and 0.75). They had shown great interest in such compositions for three way catalyst application and especially for high rate of praseodymium, such as $\text{Pr}_{0.75}\text{Zr}_{0.25}\text{O}_{2-y}$ with a reduction temperature around $T = 500$ °C and around 50% Pr reduced (variation of oxygen content: $\Delta\text{O} = 0.16$).

Bellakki *et al.*¹⁶ investigated the $\text{Pr}_{1-x}\text{Zr}_x\text{O}_{2-y}$ ($0 \leq x \leq 1$) solid solutions synthesized by the single step combustion method. They had shown by XRD investigations that this solid solution crystallizes with the fluorite-type structure from $x = 0$ to $x = 1$. H_2 -TPR measurements were performed and the higher H_2 consumptions were obtained for the Pr-rich system ($x \leq 0.5$). Finally, the achievement of pure phases is strongly related to synthesis routes.

In this study we focused on structural features and redox properties of $\text{Pr}_{1-x}\text{Zr}_x\text{O}_{2-y}$ defined compounds for high rates of praseodymium ($0.02 \leq x \leq 0.5$) and we detailed the impact of structural features and composition ($\text{Pr}^{4+}/\text{Pr}^{3+}$) on the redox properties. XRD and Zr-K-edge EXAFS investigations were first carried out. Then magnetic susceptibility measurements and Pr L_{III} -XANES studies were performed to follow the Pr oxidation states. Finally TPR and TGA measurements under Ar/5% H_2 were undertaken to evaluate the reduction properties and the reduced phases were characterized by neutron diffraction investigations.

Experimental section

Synthesis

Oxides have been prepared starting from nitrate precursors (SOLVAY), co-precipitated in basic medium (pH = 10) and annealed under air at temperatures of 700, 900 and 1200 °C for 12 hours. At pH = 10, all Pr-Zr hydroxides and oxyhydroxides precipitate. All these oxides annealed under air at 700 °C < T < 1200 °C crystallize with a fluorite-type structure and no phase transition is observed. Moreover these oxides were reduced in an oven as well as in TGA apparatus under Ar/5% H_2 flux at $T = 900$ °C in order to obtain and characterize reduced phases.

XRD analysis

Powder X-ray diffraction patterns were collected on a Phillips X'Pert MPD X-ray diffractometer with Bragg-Brentano geometry and using $\text{K}\alpha_1/\text{K}\alpha_2$ radiation ($5^\circ < 2\theta < 120^\circ$ step of 0.01° and a counting time of 150 s). Diffractograms were refined using the Rietveld method and the Fullprof package of programs with conventional reliability factors and on other hand with $\text{K}\alpha_1$ radiation ($5^\circ < 2\theta < 120^\circ$ step of 0.017° and a counting time of 1500 s) for the reduced sample exhibiting the superstructure of the fluorite-type network. Unit cell parameters, atomic positions, occupancies and Debye-Waller factors have been refined in such a case. All the diffraction patterns have

been indexed on the basis of fluorite-type structures (SG: $Fm\bar{3}m$), pyrochlore-type structures (SG: $Fd\bar{3}m$) and bixbyite-type structures (SG: $Ia\bar{3}$) in selected papers (ref. 5–10, 18–19).

Magnetic measurements

Curie constants and θ_p of various Pr-based oxides have been deduced from magnetic susceptibilities ($1/\chi = (T + \theta_p)/C$, $\chi = M/H$) with magnetization recorded between 150 K and 300 K (increment 10 K) and the magnetic field going from 0 to 50 000 Oe. Magnetic measurements have been performed on a SQUID detector magnetometer Quantum Design MPMS 5. As the Curie constant is proportional to the concentration of paramagnetic species, Pr^{3+} ($4f^2$) and Pr^{4+} ($4f^1$) contents in the various compounds can be deduced from magnetic data.

Zr K-edge EXAFS and Pr L_{III} -XANES experiments

XAFS spectra at the Zr K-edge and Pr L_{III} edge were collected on station BM23 at ESRF-Grenoble-France with beam currents between 150 mA and 250 mA. XAFS spectra were recorded at room temperature in transmission mode using a Si(111) monochromator crystal. EXAFS spectra at the Zr K-edge were reduced to normalized XAFS $\chi(k)$ using the VIPER software and weighted $k^3\chi(k)$ data using the VIPER suite of program. Least squares analysis against model environments were calculated and compared with PrO_2 , ZrO_2 and $\text{Pr}_2\text{Zr}_2\text{O}_7$ as reference compounds. Four shells have been refined leading to the determination of nine parameters (radial distance R and Debye-Waller factors $2\sigma^2$ for each shell + zero energy shift). The results obtained were compared with XRD analysis results and are reported in Table 3. In the case of Pr L_{III} XANES spectra, the Pr^{4+} and Pr^{3+} rates were estimated on the basis of reference compounds containing 100% of Pr^{4+} and 100% of Pr^{3+} .

Powder neutron diffraction study of reduced samples

$\text{Pr}_{0.98}\text{Zr}_{0.02}\text{O}_{1.51}$ oxides were characterized by powder neutron diffraction at room temperature on the 3T2 beamline with 1.2253 Å radiation and a graphite monochromator of the Léon Brillouin Laboratory (LLB) in Saclay (CEA)-France. The 2θ range was 10 – 120° with a step scan of 0.2° . Intensity treatments (profile, cell parameters, atomic positions and isotropic thermal displacement) and refinements based on the Rietveld method were performed using the Fullprof package of program. The quality of the acquisition and the refinement was based on the conventional reliability factors R_p , R_{wp} and R_{Bragg} , respectively.

TGA and TPR analyses

The thermogravimetric analysis (TGA) was carried out on a SETARAM Setsys Evolution under an Ar/3% H_2 flux (50 ml min^{-1}) with a speed rate of 5 °C min^{-1} up to $T = 900$ °C. Samples were outgassed at $T = 700$ °C for 3 hours under air without moisture in order to eliminate carbonates and residual water. Temperature programmed reduction (TPR) was performed on a Micromeritics AutoChemII under Ar/10% H_2 (25 ml min^{-1}) up to 900 °C (speed rate: 20 °C min^{-1}).

Results and discussion

XRD analysis on each sample annealed at 1200 °C, using Cu $K\alpha_1/K\alpha_2$ radiation, led to identify the single phase corresponding to the fluorite type structure (SG: $Fm\bar{3}m$) for $x = 0.02$, 0.1 and 0.2 and to the pyrochlore one (SG: $Fd\bar{3}m$) for $x = 0.35$, 0.4 and 0.5 (Fig. 1–3 and Table 1). Phase mixtures were obtained for $0.02 < x < 0.1$ (2 fluorite phases) and $0.2 < x < 0.35$ (1 fluorite and 1 pyrochlore phases). The cell parameter of $Pr_{1-x}Zr_xO_{2-y}$ compounds decreases gradually with the Zr content (Fig. 4).

Magnetic measurements were performed on the single phase with $Pr_{1-x}Zr_xO_{2-y}$ compositions and the linear variation of the inverse magnetic susceptibility *versus* temperature (Fig. 5 and Table 2) allowed determining the effective magnetic moment per Pr ion. Taking into account the theoretical effective magnetic moments of pure Pr^{4+} and Pr^{3+} compo-

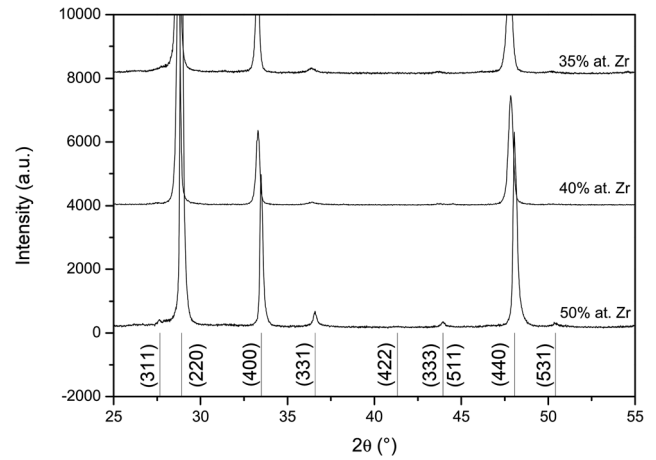


Fig. 3 Powder XRD patterns of $Pr_{1-x}Zr_xO_{2-y}$ annealed at 1200 °C under air (pyrochlore hkl planes, $a_{\text{pyrochlore}} = 2a_{\text{fluorite}}$).

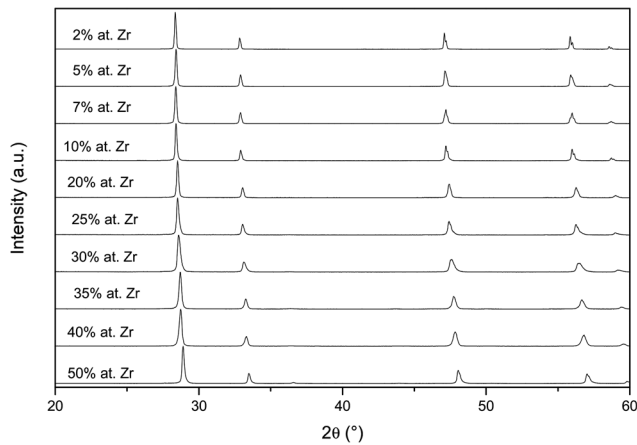


Fig. 1 Powder XRD patterns of $Pr_{1-x}Zr_xO_{2-y}$ ($0.02 < x < 0.5$) annealed at 1200 °C under air.

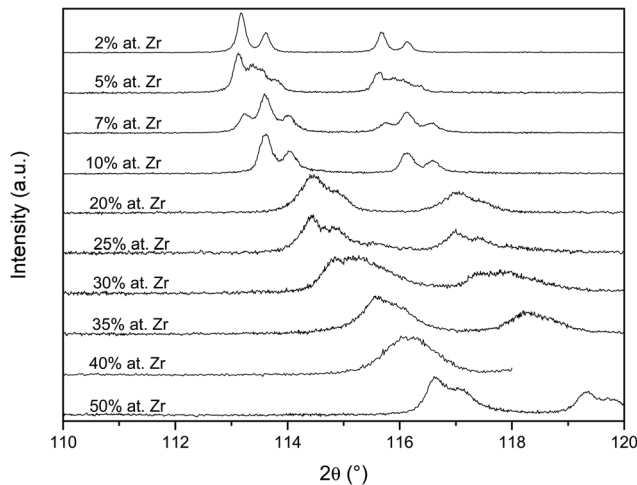


Fig. 2 Enlargement at high 2θ values of powder XRD patterns of $Pr_{1-x}Zr_xO_{2-y}$ annealed at 1200 °C under air ($0.02 < x < 0.5$).

Table 1 Compositions, structures, and refined cell parameters (compounds annealed at $T = 1200$ °C under air)

x	Structure	a (Å)	
		1st phase	2nd phase
0.02	Fluorite	5.462(3)	—
0.05	2 Fluorites	5.456(2)	5.465(2)
0.07	2 Fluorites	5.446(2)	5.458(2)
0.1	Fluorite	5.443(2)	—
0.2	Fluorite	5.421(2)	—
0.25	Fluorite + pyrochlore	5.417(2)	10.805(2)
0.3	Fluorite + pyrochlore	5.406(2)	10.772(2)
0.35	Pyrochlore	10.770(2)	—
0.4	Pyrochlore	10.738(1)	—
0.5	Pyrochlore	10.708(2)	—

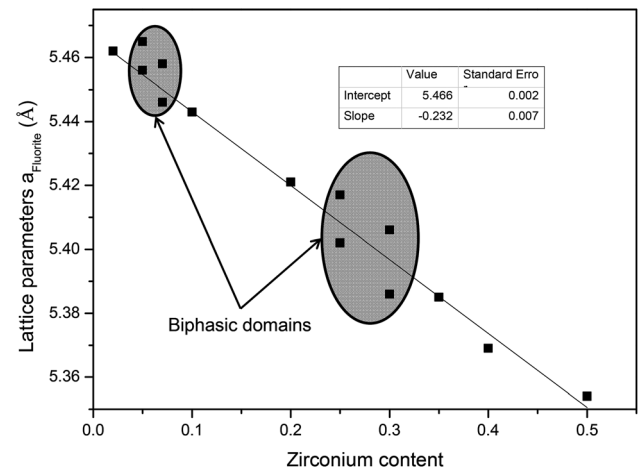


Fig. 4 Plot of lattice (fluorite) parameter a *versus* Zr content (annealed at 1200 °C under air).

sitions equal to $2.54\mu_B$ and $3.58\mu_B$, respectively, a proportion of Pr^{4+} and Pr^{3+} ions can then be evaluated in $Pr_{1-x}Zr_xO_{2-y}$ compounds. Furthermore taking into account that the theoret-

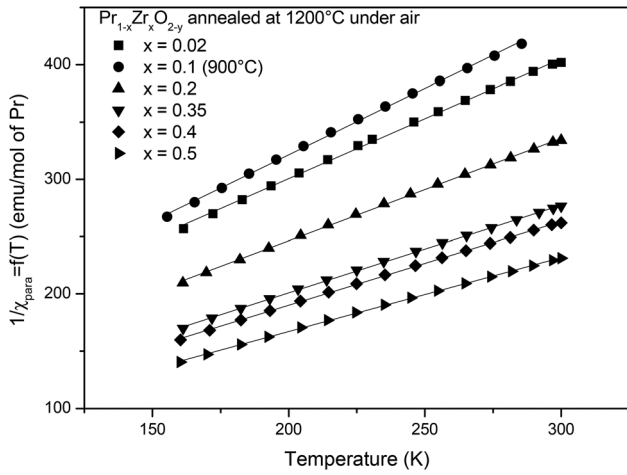


Fig. 5 Temperature dependence of the inverse magnetic susceptibility for $\text{Pr}_{1-x}\text{Zr}_x\text{O}_{2-y}$ compound annealed at 1200 °C under air.

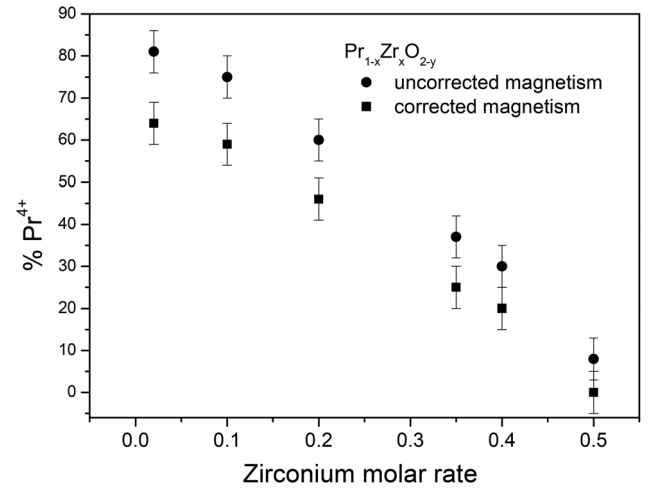


Fig. 6 Variation of Pr^{4+} concentration versus Zr^{4+} content (annealed at 1200 °C under air).

tical effective magnetic momentum of isolated ions (Pr^{4+} and Pr^{3+}) does not reflect the real values in the $\text{Pr}_{1-x}\text{Zr}_x\text{O}_{2-y}$ solid solutions (L-S spin-orbit coupling effect), two extreme compositions $\text{Pr}_{0.9}\text{Zr}_{0.1}\text{O}_2$ (one redox cycling) with 100% Pr^{4+} and $\text{Pr}_2\text{Zr}_2\text{O}_7$ ($x = 0.5$) with 100% Pr^{3+} were taken as references to evaluate the $\text{Pr}^{4+}/\text{Pr}^{3+}$ corrected ratio. Furthermore, Fig. 6 indicates that the higher the Zr^{4+} content, the lower the Pr^{4+} rate. Actually, the zirconium content does involve a $\text{Pr}^{4+}/\text{Pr}^{3+}$ ratio due to competitive bounds around $\text{Zr}^{4+}/\text{Pr}^{3+}/\text{Pr}^{4+}$, *i.e.* the ionic radii of each cation in specific six-fold, seven-fold and eight-fold oxygen environments. The larger $\text{Pr}^{3+}-\text{O}^{2-}$ bond is compensated by the smaller $\text{Zr}^{4+}-\text{O}^{2-}$ bond distance leading to the creation of oxygen vacancies.

The zirconium coordination number in the ideal pyrochlore structure ($\text{Pr}_2\text{Zr}_2\text{O}_7$, pure Pr^{3+}) is 6. Due to the partial oxidation of pyrochlore leading to the stabilization of $\text{Pr}_2\text{Zr}_2\text{O}_{7+x}$, the coordination number of Zr^{4+} changes from 6 to 7 then to 8.¹⁷ For $x = 0.2$ in the case of the oxidized and reduced phases, the Zr^{4+} coordination number seems to slightly decrease from a value between six and seven to six-fold coordination with an average Zr-O distance around 2.10 Å according to the Zr K-edge EXAFS study (Fig. 7 and Table 3). For $x = 0.5$, the

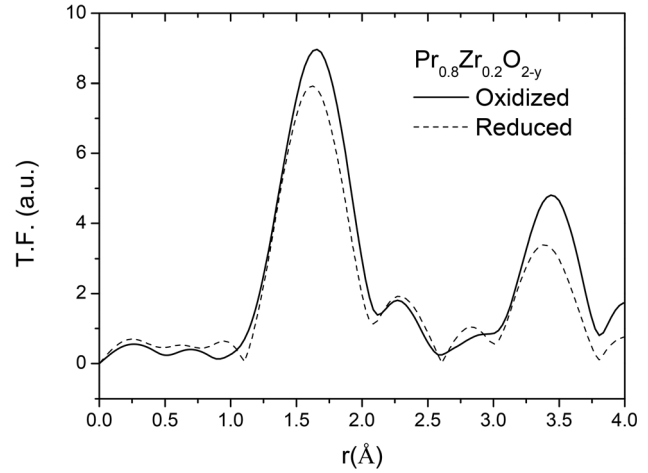


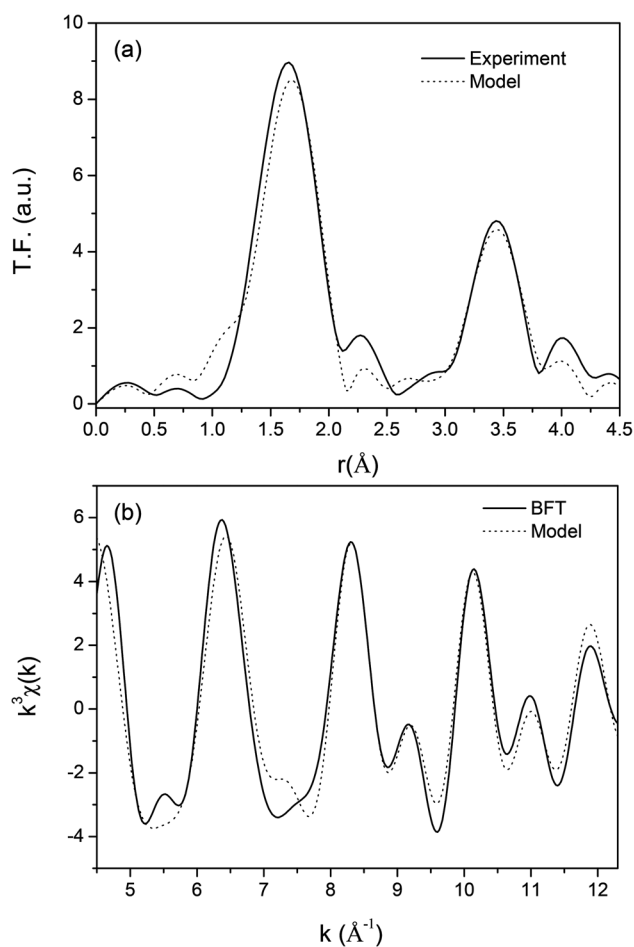
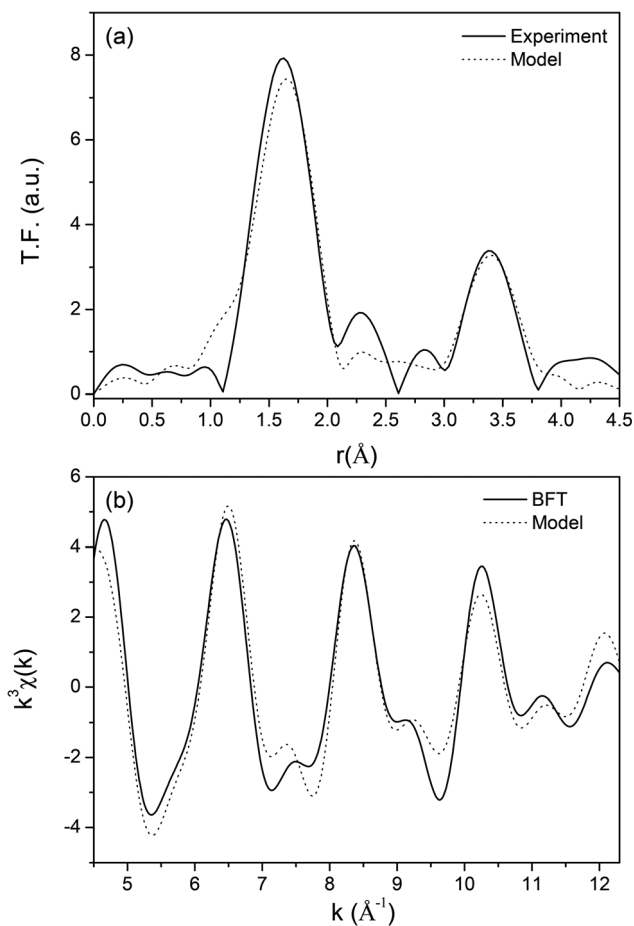
Fig. 7 Zr-K edge EXAFS spectral comparison of $\text{Pr}_{0.8}\text{Zr}_{0.2}\text{O}_{2-y}$ compound annealed at 1200 °C and annealed at 700 °C then reduced under Ar/H_2 (3%) (TGA).

Table 2 Determination of magnetic parameters corresponding to the Curie-Weiss law ($1/\chi = (T + \theta p)/C$) and the Pr oxidation state in $\text{Pr}_{1-x}\text{Zr}_x\text{O}_{2-y}$ ($0.02 < x < 0.5$) compounds annealed at 1200 °C under air

x	Thermal treatment	Slope	θp	Curie constant/Pr moles	μ_{eff} (Pr)	% Pr^{4+}	% Pr^{4+} corrected
Pr^{4+} theoretical	—	—	—	0.806	2.54 β	100	—
$\text{Pr}_{0.98}\text{Zr}_{0.02}\text{O}_{2-y}$	1200 °C	1.04 ± 0.01	-91 ± 3	0.96	2.77 β	81 ± 5	64 ± 5
$\text{Pr}_{0.98}\text{Zr}_{0.02}\text{O}_{2-y}$	700 °C	1.18 ± 0.01	-100 ± 3	0.84	2.59 β	95 ± 5	77 ± 5
$\text{Pr}_{0.9}\text{Zr}_{0.1}\text{O}_{2-y}$	1200 °C	1.00 ± 0.01	-92 ± 3	1.00	2.83 β	75 ± 5	59 ± 5
$\text{Pr}_{0.9}\text{Zr}_{0.1}\text{O}_{2-y}$	1 Redox cycle	1.58 ± 0.01	-150 ± 3	0.63	2.24 β	—	100 ± 5
$\text{Pr}_{0.9}\text{Zr}_{0.1}\text{O}_{2-y}$	900 °C	1.16 ± 0.01	-80 ± 3	0.86	2.62 β	93 ± 5	75 ± 5
$\text{Pr}_{0.8}\text{Zr}_{0.2}\text{O}_{2-y}$	1200 °C	0.894 ± 0.005	-67 ± 2	1.12	2.99 β	60 ± 5	46 ± 5
$\text{Pr}_{0.8}\text{Zr}_{0.2}\text{O}_{2-y}$	700 °C	1.15 ± 0.01	-86 ± 3	0.86	2.62 β	92 ± 5	75 ± 5
$\text{Pr}_{0.65}\text{Zr}_{0.35}\text{O}_{2-y}$	1200 °C	0.764 ± 0.004	-48 ± 1	1.31	3.24 β	37 ± 5	25 ± 5
$\text{Pr}_{0.6}\text{Zr}_{0.4}\text{O}_{2-y}$	1200 °C	0.734 ± 0.004	-44 ± 1	1.36	3.29 β	30 ± 5	20 ± 5
$\text{Pr}_{0.5}\text{Zr}_{0.5}\text{O}_{2-y}$	1200 °C	0.647 ± 0.003	-38 ± 1	1.54	3.51 β	8 ± 5	0 ± 5
Pr^{3+} theoretical	—	—	—	1.602	3.58 β	0	—

Table 3 EXAFS Zr K-edge refinement results for the two first shells

Distances	Refined parameters	$x = 0.5$	$x = 0.2$	$x = 0.1$	$x = 0.2$ reduced	$x = 0.02$
Zr-O	E_0	-7.5	-7.9	-8.2	-10.3	-4.2
	n_1	6	6	6	6	7
	r_1 (Å)	2.101(4)	2.113(5)	2.114(5)	2.090(7)	2.128(6)
Zr-Pr ⁴⁺	$2\sigma_1$ (Å ²)	0.0056(5)	0.0065(6)	0.0062(6)	0.0076(8)	0.0056(7)
	n_2	—	4.8	6.6	1.2	8
	r_2 (Å)	—	3.65(1)	3.708(8)	3.79(1)	3.72(2)
Zr-Pr ³⁺	$2\sigma_2$ (Å ²)	—	0.011(1)	0.0116(9)	0.003(1)	0.014(2)
	n_3	6	4.8	5.4	8.4	4
	r_3 (Å)	3.814(3)	3.88(2)	3.97(2)	4.07(6)	4.01(1)
Zr-Zr	$2\sigma_3$ (Å ²)	0.0043(3)	0.014	0.023(2)	0.025(8)	0.0062(9)
	n_4	6	2.4	—	2.4	—
	r_4 (Å)	3.807(5)	3.881(8)	—	3.796(7)	—
	$2\sigma_4$ (Å ²)	0.0072(3)	0.0049(7)	—	0.0039(7)	—


Fig. 8 EXAFS Zr K edge refinement of $\text{Pr}_{0.8}\text{Zr}_{0.2}\text{O}_{2-y}$ annealed at 1200 °C. Fourier transform (above) and back Fourier transform (below).

Fig. 9 Zr-K edge EXAFS refinement of $\text{Pr}_{0.8}\text{Zr}_{0.2}\text{O}_{2-y}$ annealed at 700 °C under air then reduced under Ar/H_2 (3%) (TGA). Fourier transform (above) and back Fourier transform (below).

pyrochlore phase, Zr^{4+} occupies an octahedral site at a slightly shorter Zr-O radial distance than $x = 0.2$ composition in the oxidized state. Actually, Zr-K edge EXAFS refinements (Fig. 8 and 9, Table 3) of both of these compounds with $x = 0.2$ (oxidized and reduced states) show the same number of neighbors for the first shell but a smaller Zr-O radial distance for the reduced compound. The intensity of the modulus of the

Fourier transform of the EXAFS oscillations corresponding to the first Zr-O shell increases indeed in the case of the oxidized sample. Furthermore, the Debye-Waller corresponding to the first Zr-O shell decreases for the oxidized compound leading to consider that the real average coordination number is between 6 and 7. As far as the second shells are concerned, one should have to point out that the number of neighbors of

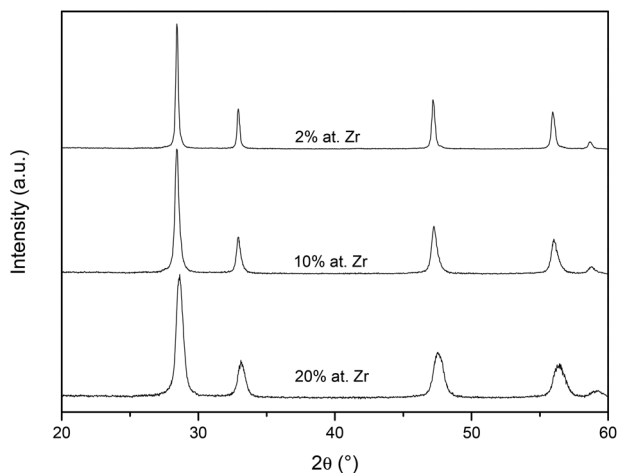


Fig. 10 Powder XRD patterns of $\text{Pr}_{1-x}\text{Zr}_x\text{O}_{2-y}$ ($x = 0.02, 0.1$ and 0.2) annealed at $700\text{ }^\circ\text{C}$ under air.

Zr- Pr^{4+} and Zr- Pr^{3+} at larger distance has been fixed at the correct value on the basis of magnetic measurements and the relative proportions of $\text{Pr}^{4+}/\text{Pr}^{3+}$ in the oxidized and reduced samples. Moreover, one should have to note that the radial distances corresponding to the second shells increase in the reduced samples in good agreement with the XRD data refinements and the increase of the cell parameter.

Eyring *et al.*¹⁴ highlighted the occurrence of defined compounds for PrO_y compositions; the same phenomenon seems to appear in $\text{Pr}_{1-x}\text{Zr}_x\text{O}_{2-y}$ solid solution, but in this case the stabilization of compounds with specific $\text{Pr}^{4+}/\text{Pr}^{3+}$ ratio can be tuned by the zirconium molar concentration.

XRD patterns of $\text{Pr}_{1-x}\text{Zr}_x\text{O}_{2-y}$ annealed at $700\text{ }^\circ\text{C}$ ($x = 0.2, 0.1$ and 0.02) are represented in Fig. 10. In this case, the lowest annealing temperature has been considered in order to evaluate the redox properties of compounds exhibiting the lowest crystallinity related to the highest surface areas and reactivity. Fig. 11 shows the H_2 -TPR profiles of $\text{Pr}_{1-x}\text{Zr}_x\text{O}_{2-y}$ annealed at $700\text{ }^\circ\text{C}$ ($x = 0.2, 0.1$ and 0.02). For these annealing temperatures, pure phases were obtained as can be seen from Fig. 10. Total hydrogen uptakes were deduced from the integrated values (from $T = 30\text{ }^\circ\text{C}$ to $900\text{ }^\circ\text{C}$) and are given in Table 4. The $\text{Pr}_{0.98}\text{Zr}_{0.02}\text{O}_{2-y}$ compound was reduced below $600\text{ }^\circ\text{C}$ and the H_2 volume uptake corresponds to reduction of 73% of Pr^{4+}

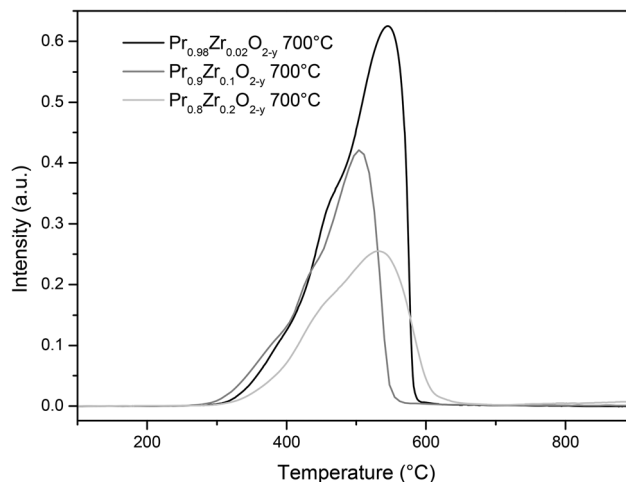


Fig. 11 H_2 -TPR profiles of $\text{Pr}_{1-x}\text{Zr}_x\text{O}_{2-y}$ for $x = 0.02, 0.1$ and 0.2 annealed at $700\text{ }^\circ\text{C}$ under air.

taking into account that 77% of Pr^{4+} was titrated in the pristine material. TGA measurement ($\text{Ar}/3\%\text{H}_2$) confirms (Fig. 12 and Table 4) the reduction steps at $250\text{ }^\circ\text{C}$, $350\text{ }^\circ\text{C}$, $450\text{ }^\circ\text{C}$ and $500\text{ }^\circ\text{C}$ of $\text{Pr}_{1-x}\text{Zr}_x\text{O}_{2-y}$ oxides. The lower temperature reduction was obtained for $\text{Pr}_{0.8}\text{Zr}_{0.2}\text{O}_{2-y}$ and $\text{Pr}_{0.9}\text{Zr}_{0.1}\text{O}_{2-y}$ compounds (below $500\text{ }^\circ\text{C}$) while H_2 uptake corresponds to reduction of only 53% of Pr^{4+} (in the case of $\text{Pr}_{0.9}\text{Zr}_{0.1}\text{O}_{2-y}$ oxide) taking into account that 75% of Pr^{4+} was stabilized in the oxidized phase (Table 4). As the Zr content increases, the Pr^{4+} reducible rate decreases because of the stabilization of high Pr^{3+} content in the pristine phase. Since the surface areas were quite low ($<10\text{ m}^2\text{ g}^{-1}$), it is assumed that the different reduction processes were not due to the surface but due to bulk phenomena and most probably due to various reduced phases with different cationic and oxygen ordering. Then, various coordination numbers from 6 to 8 for $\text{Pr}^{4+}/\text{Pr}^{3+}/\text{Zr}^{4+}$ cations can be stabilized in these reduced phases related to oxygen departure along $\langle 111 \rangle$ and $\langle 110 \rangle$ directions of the cubic fluorite-type structure.

Pr-L_{III} XANES spectra in Fig. 13 and 14 of $\text{Pr}_{1-x}\text{Zr}_x\text{O}_{2-y}$ annealed at $1200\text{ }^\circ\text{C}$ ($x = 0.2$ oxidized and reduced states, 0.1 and 0.02) illustrate the variation of Pr valence states with the two lines (5970 eV and 5981 eV with $4f^2$ and $4f^1$ electronic con-

Table 4 Compositions, refined cell parameters, Pr^{4+} rates, H_2 -uptakes (TPR measurements), $\Delta m/m$ (%), TGA measurements) and final compositions after reduction (compounds annealed at $T = 700\text{ }^\circ\text{C}$ under air)

Compositions	$\text{Pr}_{0.98}\text{Zr}_{0.02}\text{O}_{2-y}$	$\text{Pr}_{0.9}\text{Zr}_{0.1}\text{O}_{2-y}$	$\text{Pr}_{0.8}\text{Zr}_{0.2}\text{O}_{2-y}$
Deduced oxidized formulae	$(\text{Pr}_{0.77}^{4+}\text{Pr}_{0.23}^{3+})_{0.98}\text{Zr}_{0.02}^{4+}\text{O}_{1.89}$	$(\text{Pr}_{0.75}^{4+}\text{Pr}_{0.25}^{3+})_{0.9}\text{Zr}_{0.1}^{4+}\text{O}_{1.89}$	$(\text{Pr}_{0.75}^{4+}\text{Pr}_{0.25}^{3+})_{0.8}\text{Zr}_{0.2}^{4+}\text{O}_{1.9}$
TPR			
$\nu(\text{H}_2)$	2070	1430	1125
ΔO	0.36	0.24	0.18
Deduced reduced formulae	$(\text{Pr}_{0.04}^{4+}\text{Pr}_{0.96}^{3+})_{0.98}\text{Zr}_{0.02}^{4+}\text{O}_{1.53}$	$(\text{Pr}_{0.22}^{4+}\text{Pr}_{0.78}^{3+})_{0.9}\text{Zr}_{0.1}^{4+}\text{O}_{1.65}$	$(\text{Pr}_{0.3}^{4+}\text{Pr}_{0.7}^{3+})_{0.8}\text{Zr}_{0.2}^{4+}\text{O}_{1.72}$
ATG			
$\Delta m/m$ (%)	-3.06	-2.8	-2.71
ΔO	0.32	0.29	0.27
Deduced reduced formulae	$(\text{Pr}_{0.12}^{4+}\text{Pr}_{0.88}^{3+})_{0.98}\text{Zr}_{0.02}^{4+}\text{O}_{1.57}$	$(\text{Pr}_{0.12}^{4+}\text{Pr}_{0.88}^{3+})_{0.9}\text{Zr}_{0.1}^{4+}\text{O}_{1.6}$	$(\text{Pr}_{0.18}^{4+}\text{Pr}_{0.82}^{3+})_{0.9}\text{Zr}_{0.1}^{4+}\text{O}_{1.63}$

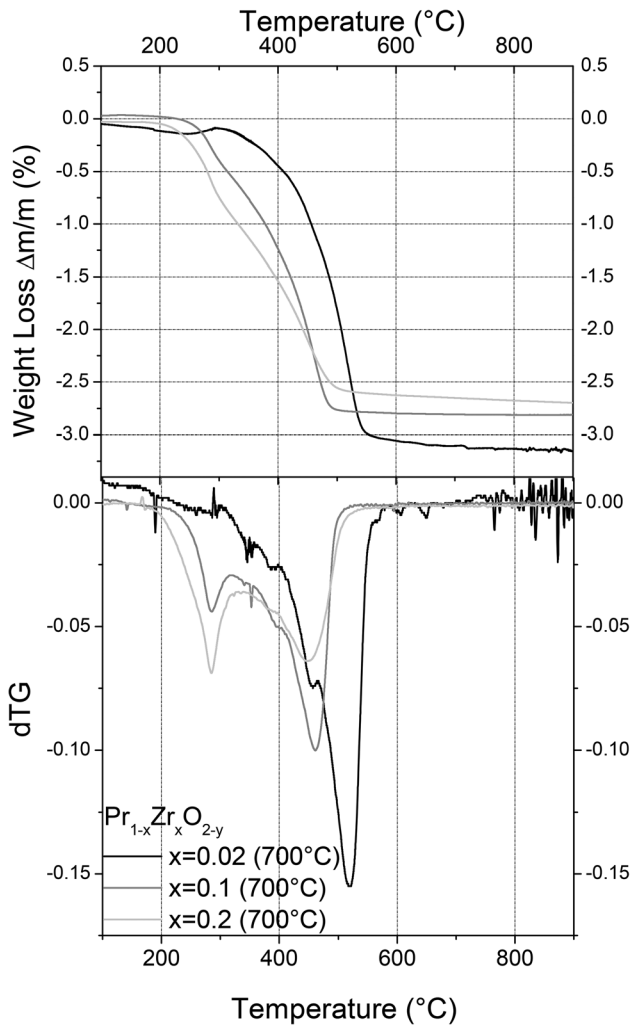


Fig. 12 Thermogravimetric curve (TG) and its first derivative (dTG) obtained for the $\text{Pr}_{1-x}\text{Zr}_x\text{O}_{2-y}$ compounds ($x = 0.02, 0.1$ and 0.2) annealed at $700\text{ }^\circ\text{C}$ under air and reduced under $\text{Ar}/3\% \text{H}_2$ atmosphere.

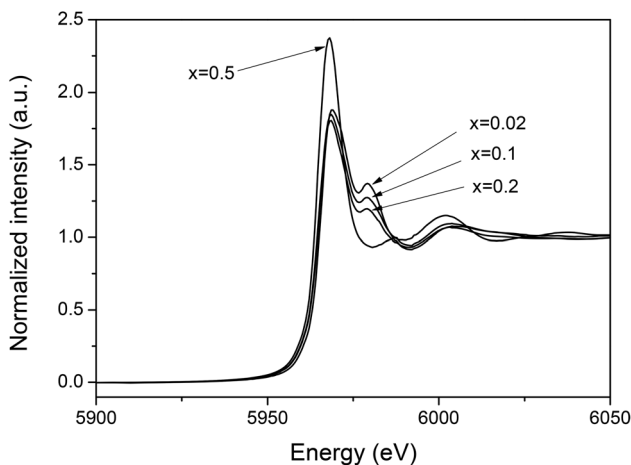


Fig. 13 Pr-L_{III} edge XANES spectra of $\text{Pr}_{1-x}\text{Zr}_x\text{O}_{2-y}$ annealed at $1200\text{ }^\circ\text{C}$ under air.

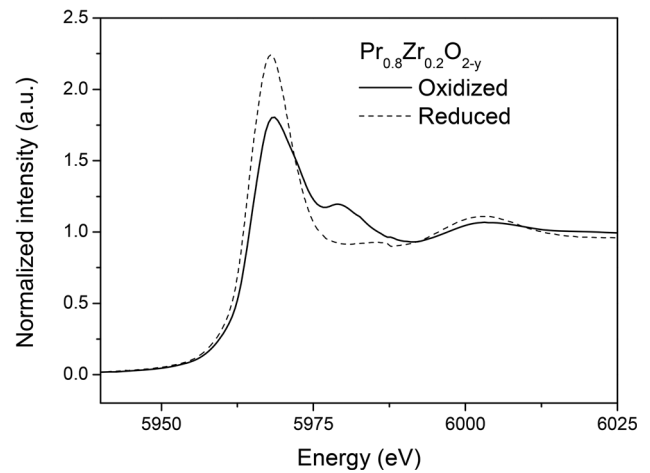


Fig. 14 L_{III} edge Pr XANES spectra of $\text{Pr}_{0.8}\text{Zr}_{0.2}\text{O}_{2-y}$ annealed at $1200\text{ }^\circ\text{C}$ under air (oxidized) and annealed at $700\text{ }^\circ\text{C}$ under air and then reduced under Ar/H_2 (3%) (TGA).

figurations of Pr^{3+} and Pr^{4+} respectively) and the increase of shake-down satellite (5981 eV) with the Pr^{4+} content.

$\text{Pr}_{0.98}\text{Zr}_{0.02}\text{O}_{2-y}$ composition annealed at $900\text{ }^\circ\text{C}$ has been reduced under Ar/H_2 (5%) at $900\text{ }^\circ\text{C}$ for 15 hours. XRD and neutron diffraction experiments were performed (Fig. 15 and Table 5). The XRD and neutron patterns could be refined using the $Ia\bar{3}$ space group; cations occupy two 24d and 8b Wyckoff positions and anions occupy 48e Wyckoff positions. The 8b sites correspond to a flattened octahedral site with six equal Pr-O bond distances, whereas the 24d sites correspond to a distorted octahedral environment with three kinds of Pr-O bond distances (Table 3). Depending on the composition, the 16c Wyckoff position could be occupied by oxygen atoms; in our case, the latter is empty leading to oxygen vacancy ordering.

The RE_2O_3 sesquioxides adopt three allotropic forms:

- A-form RE_2O_3 , with $\text{RE} = \text{La-Nd}$ seven-fold coordinated to oxygen leading to the monocapped octahedral site (the most stable thermodynamically).
- B-form RE_2O_3 , with $\text{RE} = \text{Sm-Dy}$ six-fold and seven-fold coordinated to oxygen leading to an octahedron and monocapped trigonal prisms.
- C-form, with $\text{RE} = \text{Nd-Lu}$ six-fold coordinated to oxygen leading to an octahedron and distorted trigonal prism.

Under our synthesis conditions, despite the large Pr content, the C-form corresponding to the reduced phase is always stabilized.

To conclude, investigations of reduced phases, where cationic as well as oxygen/vacancy ordering appears, show as observed for the pyrochlore network¹⁷⁻¹⁹ the stabilization of the superstructure of the fluorite-type network. Such a phenomenon should explain the high oxygen mobility as well as the high oxygen vacancy rate and reduced cation content observed in such oxides.

Moreover, smaller Zr^{4+} cations can be stabilized by larger $\text{Pr}^{(3+n)+}$ cations in its nearest neighborhood. Both these

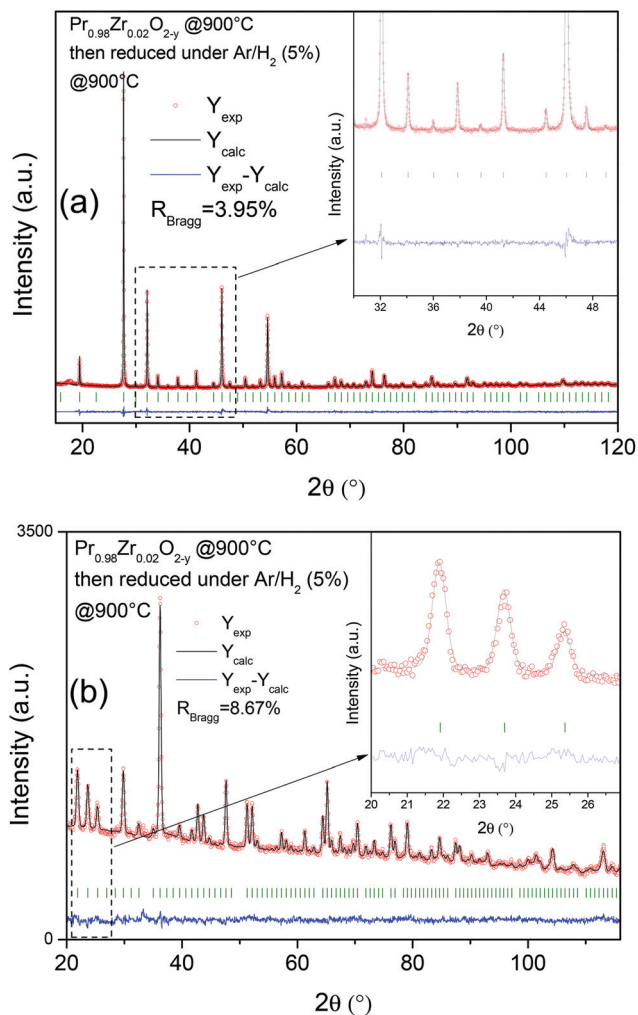


Fig. 15 Observed, calculated and difference XRD (a) and neutron (b) diffraction patterns (Rietveld) of $\text{Pr}_{0.98}\text{Zr}_{0.02}\text{O}_{1.51}$ annealed at 900 °C under air and then reduced at 900 °C under Ar/H_2 (5%).

Table 5 Atomic coordinates, isotropic thermal displacements, reliability factors and Pr–O distances for $\text{Pr}_{0.98}\text{Zr}_{0.02}\text{O}_{1.51}$ annealed at 900 °C under air then reduced at 900 °C under Ar/H_2 (5%)

Composition $\text{Pr}_{0.98}\text{Zr}_{0.02}\text{O}_{1.51}$ $a = 11.1337(4)$ Å SG: $Ia\bar{3}$						
Atoms	Sites	x	y	z	B (Å ²)	
Pr1	24d	-0.0281(5)	0	0.25	0.6(1)	
Pr2	8b	0.25	0.25	0.25	0.6(1)	
O	48e	0.3887(5)	0.1490(5)	0.3792(5)	0.83(5)	
$R_p = 21.4\%$ & $R_{wp} = 15.4\%$ & $R_{Bragg} = 8.67\%$ & $\chi^2 = 1.56$.						
Distance Pr1–O (Å)		$2 \times 2.451(4)$	$2 \times 2.384(4)$	$2 \times 2.355(4)$		
Distance Pr2–O (Å)		$6 \times 2.391(3)$				

environments are distorted. 8-fold coordinated Pr^{4+} in the cubic environment which is highly reducible appears then probably far from Zr^{4+} cations. So the oxygen release around Pr^{4+} and migration of oxygen vacancies near Zr^{4+} are assisted by the gradual variation of the Pr valence state in this series.

Conclusions

In this paper, we have explained the cell parameter variation versus the Zr content in the $\text{Pr}_{1-x}\text{Zr}_x\text{O}_{2-y}$ oxides for high content of $\text{Pr}^{4+}/\text{Pr}^{3+}$ cations. The higher the Zr content, the higher the Pr^{3+} rates in this series, thanks to competitive bonds around Zr^{4+} cations and O^{2-} anions. The occurrence of defined compositions as shown by Leroy Eyring *et al.* in the $\text{Pr}_n\text{O}_{2n-2m}$ series is associated with the accurate amount of Zr^{4+} cations stabilized in eight, seven as well as six-fold coordination sites and the existence of oxygen vacancies. The stabilization of Zr^{4+} in flattened octahedral sites as shown by EXAFS investigation at the Zr K-edge is probably a key feature for the highest Zr content (atomic% Zr > 0.1) which explains the generation of oxygen vacancies around Zr^{4+} centers and the migration of these vacancies allowing fast kinetics during the reduction steps of Pr^{4+} cations. Magnetic measurements and Pr L_{III}-edge XANES analysis give a perfect view of the variation of the $\text{Pr}^{4+}/\text{Pr}^{3+}$ rate for the oxidized and reduced phases. The occurrence of a superstructure for the reduced oxides is also an important point leading to high OSC and high content of reducible Pr^{4+} cations. TGA and TPR measurements show low first temperature reduction around $T = 250$ °C for the Zr content equal to 0.1 and 0.2. Finally, other synthesis routes such as sol-gel or self-combustion should be used in order to increase the surface area and obtain high rates of reducible species at lower temperatures for automotive exhaust catalysis.

References

- 1 M. Yu. Sinev, V. Yu. Bychkov, V. N. Korchak and O. V. Krylov, *Catal. Today*, 1990, **6**, 543.
- 2 J. Kaspar, P. Fornasiero and N. Hickey, *Catal. Today*, 2003, **77**, 419.
- 3 T. Kudo and H. Obayashi, *J. Electrochem. Soc.*, 1975, **122**(1), 42.
- 4 A. Trovarelli, *Catalysis by Ceria and related materials*, Imperial College Press, 2002.
- 5 S. N. Achary, S. K. Sali, N. K. Kulkarni, P. S. R. Krishna, A. B. Shinde and A. K. Tyagi, *Chem. Mater.*, 2009, **21**, 5848–5859.
- 6 T. Sasaki, V. Ukyo, K. Kuruda, S. Arai, S. Muto and H. Saka, *J. Am. Ceram. Soc. Jpn*, 2004, **112**(8), 440–444.
- 7 M. Yashima, T. Hirose, S. Katano, Y. Susuki, M. Kakihana and M. Yoshimura, *Phys. Rev. B Cond. Mater.*, 1995, **51**, 8434–8437.
- 8 T. Omata, H. Kishimoto, S. Otsuka-Yao-Matsuo, N. Ohtori and N. Umesaki, *J. Solid State Chem.*, 1999, **147**, 573–583.
- 9 Y. Nagai, T. Yamamoto, T. Tanaka, S. Yoshida, T. Nanaka, T. Okamoto, A. Suda and M. Sugiura, *Catal. Today*, 2002, **74**, 225–234.
- 10 S. Lemaux, A. Bensaddik, A. M. J. Van der Erden, J. H. Bitter and D. C. Koningsberger, *J. Phys. Chem. B*, 2001, **105**, 4810–4815.

- 11 W. Wendong, L. Peiyan, M. Ming, F. Yilu, H. Tiandou, X. Yaning and L. Tao, *J. Rare Earths*, 2003, **21**, 430–435.
- 12 R. B. Von Dreele, L. Eyring, L. Bowman and J. L. Yarnell, *Acta Crystallogr., Sect. B: Struct. Crystallogr. Cryst. Chem.*, 1975, **31**, 971.
- 13 J. Zhang, R. B. Von Dreele and L. Eyring, *J. Solid State Chem.*, 1996, **122**, 53–58.
- 14 L. Eyring, in *Handbook on the Physics and Chemistry of Rare Earths*, ed. K. A. Gschneidner Jr. and L. Eyring, North-Holland, Amsterdam, 1979, vol. 3, p. 337.
- 15 C. K. Narula, P. Haack, W. Chun, H.-W. Jen and G. W. Graham, *J. Phys. Chem. B*, 1999, **103**, 3634.
- 16 M. B. Bellakki, C. Shivakumara, T. Baidya, A. S. Prakash, N. Y. Vasanthacharya and M. S. Hegde, *Mater. Res. Bull.*, 2008, **43**, 2658–2667.
- 17 J. B. Thomson, A. Robert Armstrong and P. G. Bruce, *J. Am. Chem. Soc.*, 1996, **118**, 11129–11133.
- 18 I. Alessandri, M. A. Bañares, L. E. Depero, M. Ferroni, P. Fornasiero, F. C. Gennari, N. Hickey, M. V. Martinez-Huerta and T. Montini, *Top. Catal.*, 2006, **41**, 35–42.
- 19 T. Montini, N. Hickey, P. Fornasiero, M. Graziani, M. A. Banares, M. V. Martinez-Huerta, I. Alessandri and L. E. Depero, *Chem. Mater.*, 2005, **17**, 1157.